Journal of Volcanology and Geothermal Research 354 (2018) 87–101

Contents lists available at ScienceDirect

Journal of Volcanology and Geothermal Research

journal homepage: www.elsevier.com/locate/jvolgeores

Invited research article

Challenging dyke ascent models using novel laboratory experiments: Implications for reinterpreting evidence of magma ascent and volcanism

Janine L. Kavanagh [a,*], Alec J. Burns [b], Suraya Hilmi Hazim [a], Elliot P. Wood [a], Simon A. Martin [a], Sam Hignett [a], David J.C. Dennis [b]

[a] Department of Earth, Ocean and Ecological Sciences, University of Liverpool, Liverpool L69 3GP, United Kingdom
[b] School of Engineering, University of Liverpool, Liverpool L69 3GH, United Kingdom

ARTICLE INFO

Article history:
Received 26 July 2017
Received in revised form 21 December 2017
Accepted 2 January 2018
Available online 6 January 2018

Keywords:
Magma flow
Host-rock deformation
Dyke
Analogue experiment
Particle image velocimetry
Digital image correlation

ABSTRACT

Volcanic eruptions are fed by plumbing systems that transport magma from its source to the surface, mostly fed by dykes. Here we present laboratory experiments that model dyke ascent to eruption using a tank filled with a crust analogue (gelatine, which is transparent and elastic) that is injected from below by a magma analogue (dyed water). This novel experimental setup allows, for the first time, the simultaneous measurement of fluid flow, sub-surface and surface deformation during dyke ascent. During injection, a penny-shaped fluid-filled crack is formed, intrudes, and traverses the gelatine slab vertically to then erupt at the surface. Polarised light shows the internal stress evolution as the dyke ascends, and an overhead laser scanner measures the surface elevation change in the lead-up to dyke eruption. Fluorescent passive-tracer particles that are illuminated by a laser sheet are monitored, and the intruding fluid's flow dynamics and gelatine's sub-surface strain evolution is measured using particle image velocimetry and digital image correlation, respectively. We identify 4 previously undescribed stages of dyke ascent. Stage 1, early dyke growth: the initial dyke grows from the source, and two fluid jets circulate as the penny-shaped crack is formed. Stage 2, pseudo-steady dyke growth: characterised by the development of a rapidly uprising, central, single pseudo-steady fluid jet, as the dyke grows equally in length and width, and the fluid down-wells at the dyke margin. Sub-surface host strain is localised at the head region and the tail of the dyke is largely static. Stage 3, pre-eruption unsteady dyke growth: an instability in the fluid flow appears as the central fluid jet meanders, the dyke tip accelerates towards the surface and the tail thins. Surface deformation is only detected in the immediate lead-up to eruption and is characterised by an overall topographic increase, with axis-symmetric topographic highs developed above the dyke tip. Stage 4 is the onset of eruption, when fluid flow is projected outwards and focused towards the erupting fissure as the dyke closes. A simultaneous and abrupt decrease in sub-surface strain occurs as the fluid pressure is released. Our results provide a comprehensive physical framework upon which to interpret evidence of dyke ascent in nature, and suggest dyke ascent models need to be re-evaluated to account for coupled intrusive and extrusive processes and improve the recognition of monitoring signals that lead to volcanic eruptions in nature.

1. Introduction

Nearly all volcanic eruptions are fed by magma-filled fractures that propagate through the crust. The dynamics and propagation of magma intrusions has direct influence on the style, longevity and climatic impact of volcanic eruptions by modulating the supply, ascent rate and rheology of magma that reaches the surface (e.g. Caricchi et al., 2014a, 2014b; Ilyinskaya et al., 2017). Magma intrusion precedes volcanic activity (e.g. Patane et al., 2002), can trigger an eruption (e.g. Sigmundsson et al., 2010), occurs during volcanism (e.g. Castro et al., 2016) and is active in repose periods between eruptions (e.g. Wright et al., 2012). The majority of dykes do not erupt (e.g. Crisp, 1984; Gudmundsson, 2002) and diverse geophysical, geochemical and geodetic techniques can be readily employed to monitor magma intrusion in the build up to and during volcanic crises, e.g. retrieving seismic profiles, recording volcanic gas emissions, and detecting surface changes in elevation as the magma-filled fractures grow (e.g. Sparks et al., 2012). However, our ability to interpret this data depends on, and is limited by, the validity of model assumptions and field observations.

Volcanic plumbing systems comprise a network of interconnected magma intrusions that vary in orientation relative to stratigraphic layering and span orders of magnitude in volume and aspect ratio (see the collection of papers in the Special Volume by Menand et al., 2011

* Corresponding author.
E-mail address: Janine.Kavanagh@liverpool.ac.uk (J.L. Kavanagh).

https://doi.org/10.1016/j.jvolgeores.2018.01.002

for a review). Dykes are vertical to sub-vertical magma-filled fractures that have high aspect ratio (length/thickness), cut across bedding planes of rock strata, and are the primary conduit to transport magma through the crust to potentially erupt (e.g. Geshi et al., 2010; Gudmundsson, 2006). The rock record provides access to ancient volcanic plumbing systems through field studies of the solidified remnants of magma and deformed surrounding host rock in 2D (e.g. Gudmundsson, 2003) and rarely in 3D (e.g. Kavanagh and Sparks, 2011). However, only a partial record will be preserved and it can be difficult to distinguish pre-, *syn*- and post-magma intrusion processes. Studying dyke propagation in nature is challenging as only remote measurements can be made during an intrusive event. Evidence of recent dyking has been garnered through geophysical and geodetic measurements of intrusions related to on-land rifting, e.g. Afar and Iceland (Wright et al., 2012). The 2014 dyke intrusion associated with the Bardarbunga volcanic system (e.g. Sigmundsson et al., 2014; Gudmundsson et al., 2014) is arguably the most detailed study of an individual dyking event that led to a fissure eruption. Along with studies of eruptive episodes on Etna, Italy (e.g. González and Palano, 2014, Kahl et al., 2011) and Kilauea, Hawaii (e.g. Cervelli et al., 2002) for example, this has done much to shape and inform our understanding of the geophysical signals of magma intrusion that leads to eruption.

Magma ascends through the crust in regional dykes from deep magma reservoirs primarily due to buoyancy; dyke ascent in nature represents the release of gravitational potential energy on a planetary scale (see Putirka, 2017 for a review) and the release of elastic energy on a regional scale. Magma ascent in dykes is facilitated or impeded by the ability of the magma to flow (its rheology) and deformation of mechanically layered and fractured crustal rocks to accommodate the intrusion. Analogue experimentation and numerical modelling are complementary methods to aid the interpretation of field studies and geophysical surveys of magma intrusion (see Rivalta et al. (2015) and Kavanagh et al. (2017b) for reviews). These dyke propagation models have considered a range of physical processes that impact dyke ascent, including magma buoyancy (e.g. Takada, 1990; Rivalta et al., 2005; Taisne and Jaupart, 2009), solidification (e.g. Taisne and Tait, 2011), deformation of the host material (e.g. Abdelmalak et al., 2012; Kavanagh et al., 2015), interaction with a load or stress field (Watanabe et al., 2002; Daniels and Menand, 2015; Menand et al., 2010; Maccaferri et al., 2014; Pinel and Jaupart, 2000), mechanical layering (e.g. Kavanagh et al., 2006) and pre-existing structures or weak boundaries (e.g. Le Corvec et al., 2013a; Kavanagh et al., 2017a). Technical challenges have meant that analogue experiments have studied either the magma or the host solid, and yet the coupled nature of dyke intrusion means that the simultaneous quantification of both aspects is needed.

In this invited paper, here we describe a new series of novel laboratory experiments where, for the first time, coupled magma flow and host rock deformation is studied during dyke initiation, propagation and eruption. By quantifying flow velocity within the analogue magma with contemporaneous surface deformation and sub-surface strain and stress evolution, we identify previously unrecognised processes that relate the interaction of the intruding magma with its host material to dyke propagation dynamics. We discuss our results in the context of monitoring magma intrusion events and the potential of the rock record to preserve both flow dynamics in crystalline fabrics and evidence of sub-surface deformation during magma intrusion. Our results challenge existing dyke models that are used to interpret surface deformation related to magma intrusion that leads to eruption.

2. Experimental setup and data processing methods

2.1. Gelatine preparation, Young's modulus measurement and scaling

To prepare an experiment, forty litres of 2.5 wt% concentration gelatine was made following the guidelines of Kavanagh et al. (2013). To dissolve the mixture, one kilogram of gelatine powder (260 Bloom, 10 mesh, pig-skin gelatine supplied by Gelita UK) was mixed with 19 kg distilled water at approximately 90 °C, and this was then diluted further by 20 kg of cold distilled water to create the final desired concentration. Distilled water was used to inhibit bacterial growth and to ensure no impact of local water composition on the gelatine's properties, which has been shown to be susceptible to pH (e.g. Djabourov et al., 1988; Brizzi et al., 2016). In its sol-state (liquid), the hot gelatine mixture was poured into a clear-Perspex square-based tank measuring 40 × 40 × 30 cm^3 (see Fig. 1), any bubbles were then removed from the surface, and the surface was covered in a thin layer of oil to stop dehydration and the development of a tough 'skin'. The experiment tank was then covered in a layer of plastic-wrap and placed into a refrigerator at 5 °C to cool and solidify for approximately 20 h (see Table 1).

The Young's modulus of the gelatine solid was measured immediately prior to running an experiment. To do this the experiment tank was taken out of the refrigerator and the plastic wrap and oil layer was removed. A brass cylindrical load (see Table 2) was then placed in centre of the gelatine's surface, and the deflection it caused was measured using a digital micrometer. Following the guidelines from Kavanagh et al. (2013), the diameter of the load was small compared to that of the experiment tank, and the mass was sufficient to cause a measureable deflection (±0.005 mm). The Young's modulus E was then calculated using the following equation (Kavanagh et al., 2013):

$$E = \frac{mg(1-\nu^2)}{D\omega} \quad (1)$$

where m is the mass of the experiment load, g is gravity, ν is Poisson's ratio of the gelatine (0.5, according to Righetti et al., 2004), D is the load diameter and ω is the deflection it causes to the gelatine's surface. For each experiment, an average of measurements is reported (Table 1) based on two different loads (Table 2) and three measurements per load.

Kavanagh et al. (2013) showed that gelatine mixtures in the gel-state (2–5 wt% and 5–10 °C) that are injected by water can be appropriately scaled to model dyke propagation in nature. They defined a series of scale factors based on the assumption that the characteristic length scale of the experiment is the buoyancy length L_b, which is the length of the fracture when the buoyancy forces balance the resistive forces of the fracture (Taisne and Tait, 2009):

$$L_b = \left(\frac{K_c}{\Delta\rho}\right)^{\frac{2}{3}}, \quad (2)$$

where K_c is the fracture toughness and $\Delta\rho$ is the density difference between the intruded fluid and the host material. From this follows four scale factors (Kavanagh et al., 2013):

Length scale L*:

$$L^* = \frac{L_l}{L_n} = \left(\frac{K_c^*}{\Delta\rho^*}\right)^{\frac{2}{3}}, \quad (3)$$

Fig. 1. Schematic sketch of three apparatus setups for imaging dyke experiments where water is injected into the base of a gelatine slab using a peristaltic pump. a) Two polarising sheets (pale grey) are attached to the outside of the tank in the x-z plane. An overhead laser (L1) monitors surface elevation change along a line projected onto the sand-covered gelatine surface (x-y plane), centred on the injection point and perpendicular to the dyke strike-direction. Three HD cameras monitor the growth of the dyke (HD-1 x-z plane, HD-2 y-z plane, and HD-3 x-y plane). b) Particle image velocimetry: a CCD camera (y-z plane) records fluorescing passive-tracer particles within the injected fluid, in a vertical laser sheet projected through the gelatine (centred on the injector, and parallel to the dyke strike-direction). c) Digital image correlation: a CCD camera (x-z plane) records a vertical laser-illuminated sheet through the gelatine (centred on the injector, perpendicular to the dyke strike-direction), which contains suspended passive-tracer particles. Side (i) and plan (ii) views are shown for each method.

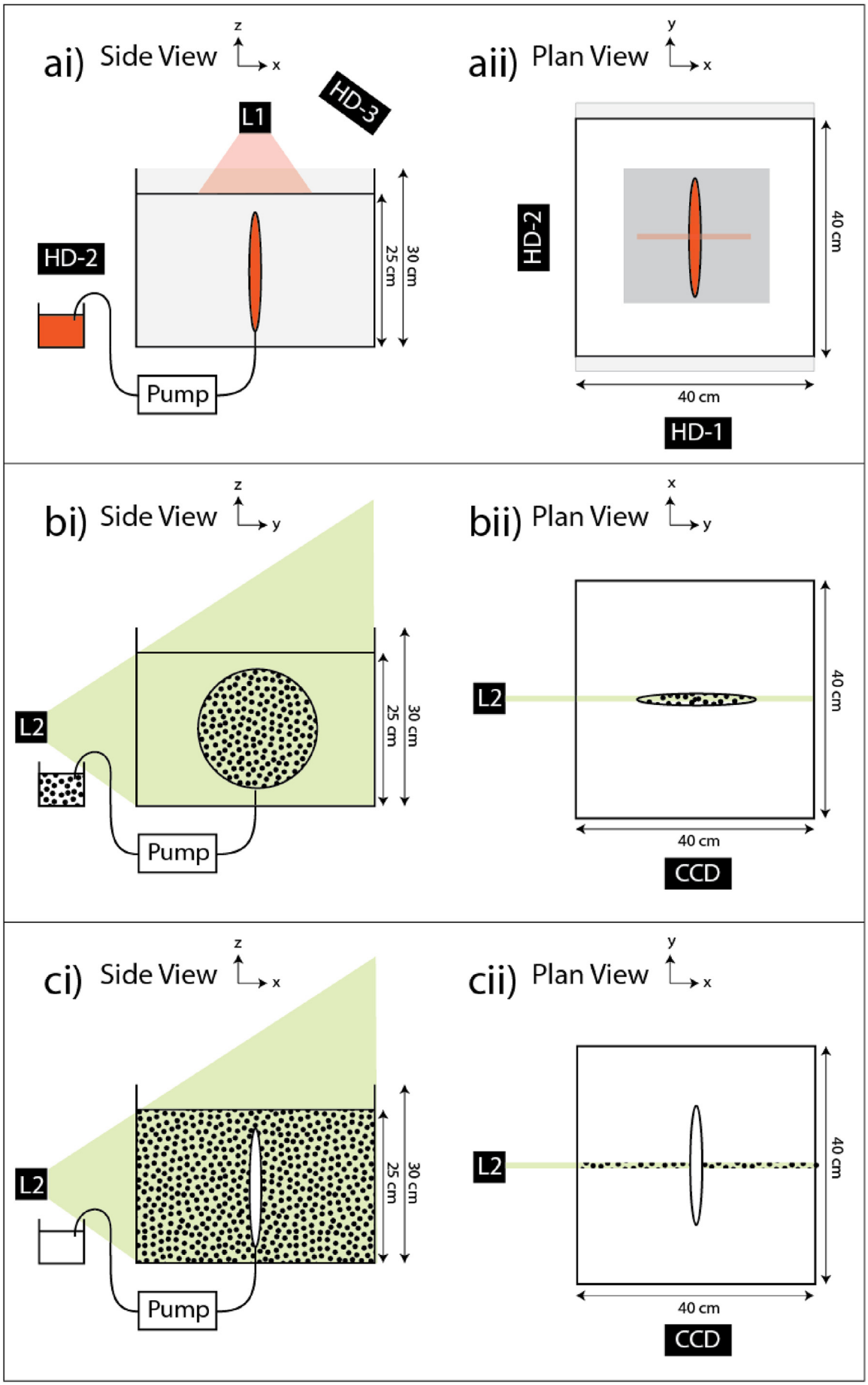
ai) Side View
z
x
HD-3
L1
HD-2
25 cm
30 cm
Pump
aii) Plan View
y
x
HD-2
40 cm
40 cm
HD-1
bi) Side View
z
y
L2
25 cm
30 cm
Pump
bii) Plan View
x
y
L2
40 cm
40 cm
CCD
ci) Side View
z
x
L2
25 cm
30 cm
Pump
cii) Plan View
y
x
L2
40 cm
40 cm
CCD

Table 1
Experiment parameters and variables. X = gelatine concentration, H = gelatine layer depth, ρ = gelatine density, T_{mix} = temperature of gelatine mixture when left to solidify, T = gelatine temperature when experiment commenced, t_{set} = time cooling, Q = injection flux, E = Young's modulus, t = time to eruption, and Technique = experimental imaging and analysis technique applied (Pol = polarised light, Surf Def = surface elevation change monitoring, PIV = particle image velocimetry, DIC = digital image correlation).

Experiment # (Ref)	X (wt%)	H (m)	ρ (kg/m^3)	T_{mix} (°C)	T (°C)	t_{set} (hr)	Q (m^3/s)	E (Pa)	t (s)	Technique
1 (SD07)	2.5	0.24	1002.5	24	5	24	3.9×10^{-7}	2921	480	Pol, Surf Def
2 (SD09)	2.5	0.24	1002.5	23	5	23	3.9×10^{-7}	3042	500	Pol, Surf Def
3 (AJB01)	2.5	0.25	1002.5	22	5	16	3.9×10^{-7}	2030	416	PIV
4 (AJB02)	2.5	0.25	1002.5	21	5	15.5	3.9×10^{-7}	2030	405	DIC

Table 2
Properties of experimental loads used to calculate Young's modulus of the solidified gelatine prior to running an experiment, where 'm' is the mass of the load and 'a' is its radius.

	Geometry	Material	m (kg)	a (m)
Load A	Cylinder	Brass	0.0501	0.0125
Load B	Cylinder	Brass	0.0418	0.0125

Timescale T*:

$$T^* = \frac{T_l}{T_n} = \rho_{solid}^{*\frac{1}{2}} K_c^{*\frac{1}{3}} (\Delta\rho)^{-\frac{5}{6}}, \quad (4)$$

Velocity scale U*:

$$U^* = \frac{U_l}{U_n} = (\Delta\rho^*)^{\frac{1}{6}} K_c^{*\frac{1}{3}} \rho_{solid}^{*-\frac{1}{2}}, \quad (5)$$

and Stress scale E*:

$$E^* = \frac{E_l}{E_n} = \Delta\rho^* L_b^* \left(\frac{L_b}{\psi}\right)^*, \quad (6)$$

where subscript l is in the laboratory, subscript n is in nature, ρ_{solid} is the density of the host material and ψ is the thickness of the intrusion. In our experiments where water is injected into gelatine: $L^* = 2 \times 10^{-3}$, and so 1 m in experimental dyke length corresponds with 500 m of dyke length in nature; $T^* = 9 \times 10^{-2}$, meaning 1 s of the experiment corresponds to 11 s in nature; and $U^* = 2 \times 10^{-2}$, such that 0.001 m/s in the experiment represents 0.05 m/s in nature. Kavanagh et al. (2013) found that $E^* = 2 \times 10^{-6}$ to 2×10^{-5}, and as our laboratory measurements of Young's modulus fall within this range and span 2000–3000 Pa (Table 1), this corresponds to rocks in nature that have a Young's modulus of 0.1–1.5 GPa. These values are geologically reasonable and so support the preface that scaled gelatine experiments can be used to describe magma intrusion in nature.

2.2. Experimental setup

An experiment is run by injecting water through the base of the solid gelatine slab, using a tapered syringe connected to a peristaltic pump that delivers fluid at a constant volumetric flux (see Table 1). A valve connected to the injection system and a small petroleum jelly seal at the injector tip ensures only water and no air is injected. The orientation of the dyke that is formed is controlled by making a small, vertical cut in the base of the gelatine and inserting the injector into this. It is ensured that the tapered edge of the injector is orientated parallel to the crack. To this basic setup, additional imaging apparatus are used and these are described in more detail in the following sub-sections. These include: gelatine stress field analysis, surface elevation change, dynamics of the intruding fluid flow using particle image velocimetry (PIV), and sub-surface strain analysis via digital image correlation (DIC).

2.2.1. Photoelasticity and surface deformation

Polarising sheets are attached to the outside of the experiment tank, on opposite sides and perpendicular to the dyke strike direction (x-z plane, see Fig. 1a). Gelatine solids are photoelastic, meaning that qualitative stresses and their evolution can be visualised using polarised light. Two light sources illuminate the tank from behind, and two HD video cameras are used to record the sub-surface growth of the experimental intrusions; one is positioned to record the polarised-light view (HD-1, x-z plane), and one images the plane of the dyke in artificial light (HD-2, y-z plane). An additional HD video camera positioned above the experiment tank monitors the free-surface of the gelatine (HD-3, x-y plane). Footage from cameras HD-1 and HD-2 was analysed using the open source software Tracker (Version 4.96) to measure the dyke length, width, and tip position relative to the surface of the gelatine over time.

To monitor the changes in surface topography over time, a Micro-Epsilon laser scanner (L1) is positioned above the analogue setup (Fig. 1a). The laser projects a thin, vertical sheet of light onto the surface of the gelatine; this produces a red line on the gelatine surface that is positioned perpendicular to the dyke strike direction and centred on the injector port. As the gelatine solid is transparent, a thin layer of dark-coloured fine sand (approximate particle size 0.25 mm) is spread evenly over the surface of the gelatine to aid deflection of the laser light. The software ScanCONTROL 5.0 is used to collect data along a 140 mm long transect, with measurement points positioned every 0.5 mm along the projection. Each point along the projection is assigned a height value that corresponds to the distance between the surface of the gelatine and the source of the laser sheet. Changes in the surface topography are recorded at timed intervals of 4 scans per second.

After the experiment, data from the Micro Epsilon laser scanner are exported and manipulated in MATLAB (by Mathworks). Sub-sampling of the dataset produces an elevation profile in 10 s intervals. The cumulative sum of displacement is then calculated across the horizontal transect to illustrate the change in topography over time. Using the statistical analysis software R, a non-parametric fit LOESS curve (Locally Weighted Scatterplot Smoothing) is applied with a span width of 0.3 for the smoothing window.

2.2.2. Particle image velocimetry (PIV) and digital image correlation (DIC)

PIV or DIC are used to quantify fluid flow velocities within the injected fluid or sub-surface strain evolution in the intruded gelatine, respectively. A New Wave Solo-PIV III Laser (L2) provides 50 mJ of energy per pulse at 15 Hz, with a pulse width of 3–5 ns and a wavelength of 532 nm. The laser fires at a repetition rate of 8.875 Hz for the PIV fluid flow experiments (Fig. 1b) and 1 Hz for the DIC gelatine sub-surface deformation experiments (Fig. 1c). The laser light is formed into a thin sheet (approximately 1 mm thick) using a cylindrical lens which excites 20–50 μm fluorescent, spherical poly(methyl methacrylate) (PMMA)

Fig. 2. Series of cropped photographs showing the evolution of stress in the gelatine during dyke ascent at 3 time steps: a) 60 s, b) 240 s, and c) 480 s. The position of the overhead laser is clear in all colour images as a red line at the top of the frame. (i) Polarised light, where the photoelasticity of gelatine produces colour fringes that relate to stress intensity, and (ii) these images converted to greyscale to show the stress pattern more clearly. (iii) A perpendicular view of the dyke growth showing the typical penny-shape. (Experiment 1; see Table 1, Fig. 1a and Supplementary Video Fig. S1).

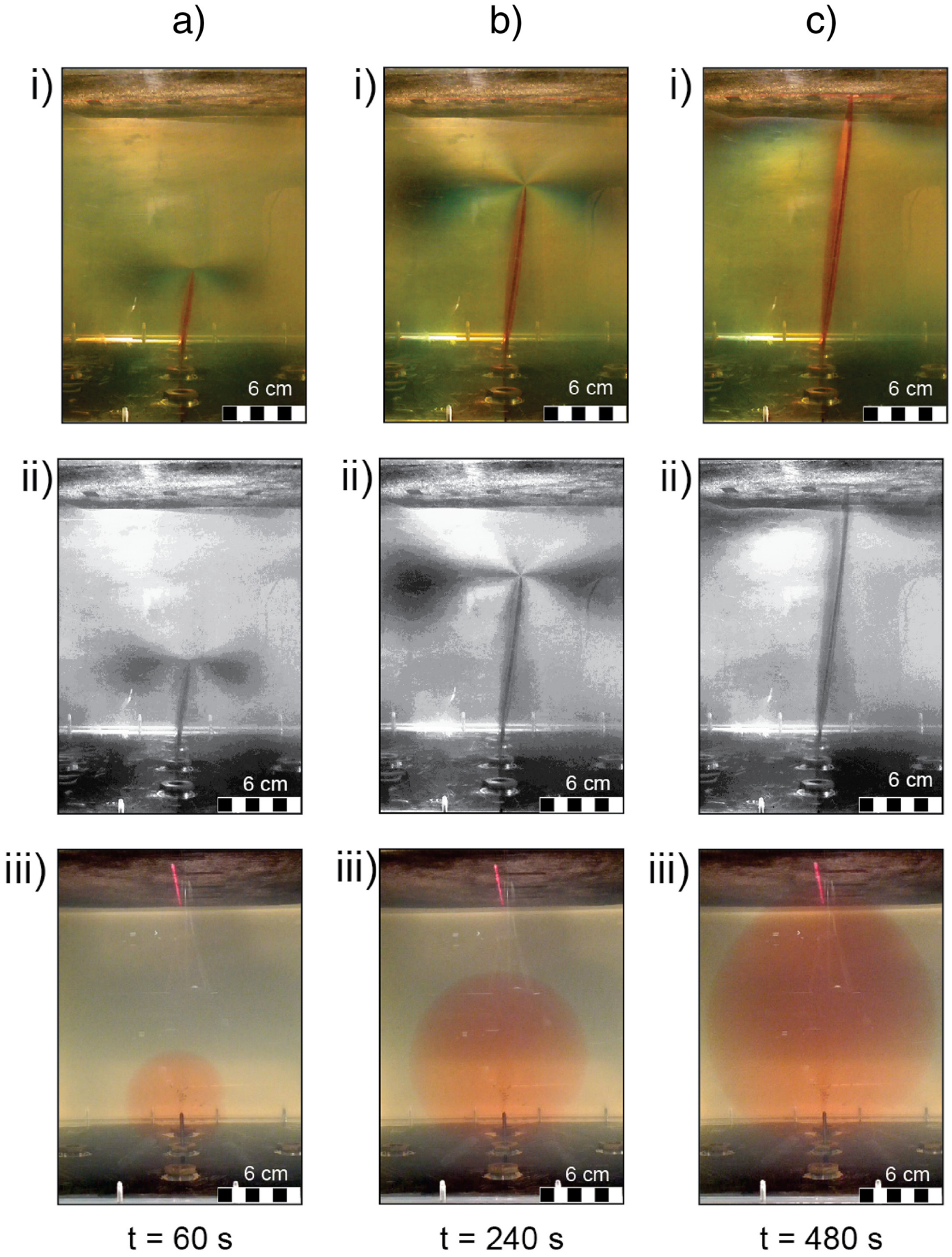
a)
b)
c)
i)
ii)
iii)
6 cm
t = 60 s
t = 240 s
t = 480 s

passive tracer particles with a Rhodamine-B coating that gives peak fluorescence at a wavelength of 590 nm. The laser sheet is fired from the side of the tank and positioned vertically so it intersects with the injection point (Fig. 1b, c).

The passive tracer particles are mixed into the injection fluid (Fig. 1b) or the host gelatine during preparation of the experiment (Fig. 1c). Particles within the injecting fluid are added immediately prior to injection, and the fluid is kept in a container placed on a magnetic stirrer to ensure they remain in suspension during extraction. The particles are slightly denser than water and so over time they settle out of suspension, although this occurs over 10's of minutes and so is beyond the time of an individual experiment. The fluorescent particles are added to the hot gelatine mixture prior to it being left to cool, stirring it continuously before being placed in the refrigerator when it reaches 21 °C. This ensures an even distribution of the tracer particles within the solidified gelatine.

Images are captured using a 2 MP CCD camera fitted with a 35 mm Nikon lens (Fig. 1b,c). The light reflected from the experiment is filtered using an optical longpass filter, which passes light with a long wavelength and blocks short wavelengths with a cut-in wavelength of 550 nm. This prevented the laser light that was reflected by the gelatine from entering the camera, thus allowing the light from the fluorescent particles to be clearly observed.

2.2.2.1. Calibration and pre-processing. Before each PIV or DIC experiment, an image is acquired of a 2D calibration target (an array of evenly-spaced black dots on a white background) aligned with the laser sheet and situated in the tank filled with water. Dantec Dynamic Studio imaging software detects the position and size of the filled-circles, and defines the area across which quantitative analysis can be accurately performed. This calibration image is later used in pre-processing to dewarp images of the experiment that are acquired. This process corrects for any distortion (which is minimal in our experiments and only occurs around the edges of the camera image; areas which are of little interest) as well as providing an accurate conversion between pixels and physical space. Great care is taken to ensure that the camera location, camera focus, tank location and laser sheet are not altered between this calibration step and the experiment itself.

2.2.2.2. Data processing and post-processing. After dewarping (described above) PIV cross-correlations produce vector fields (e.g. Adrian, 1991) using Dantec Dynamic Studio software. We utilise an adaptive correlation technique in which the interrogation windows have a 50% overlap. This results in a distance between vectors of 1.8 mm. Spurious vectors are removed using standard range and moving average validation techniques, and replaced with local mean values.

Post-processing of the vector fields is conducted in Matlab. As the region of interest increases in size throughout the experiment as the intrusion grows, we developed a masking technique that creates and applies a different mask for every PIV vector field. This is based on the region of interest being identified in the experimental images using an intensity threshold. This processing step eliminates vectors outside the region of interest that are purely the result of measurement noise.

For visualisation purposes only (figures and movies) a 3-by-3 spatial box is applied to the vector fields before plotting. In addition, it is evident that long time-averaging is not possible due to the constantly varying size of the intrusion. However, given that the timescale of the growth of the intrusion is significantly longer than the PIV capture rate we can average over a limited number of frames (10) such that each plot (or movie frame) is a short time-average (i.e. spanning 1.13 s in the PIV dyke flow experiments). Finally, to improve the clarity of the vectors in the visualisations, they are down-sampled by a factor of two (i.e. only every second vector is plotted) or three, depending on the type of experiment and visualisation. The colour-maps in all cases are not down-sampled and reflect the resolution of the experiments.

In the DIC experiments, strain is calculated from the post-processed vector field data. For the small strains in the sub-surface gelatine (significantly less than unity) the strain tensor can be linearised to give Cauchy's infinitesimal strain tensor:

$$\epsilon_{ij} = \frac{1}{2}\left(\frac{\partial \mathbf{v}_i}{\partial \mathbf{x}_j} + \frac{\partial \mathbf{v}_j}{\partial \mathbf{x}_i}\right), \tag{7}$$

where $\mathbf{v}$ is the displacement vector, and $\mathbf{x}$ is the spatial coordinate. Thus, in the two-dimensions of interest in the DIC experiments, u and w are vector displacements in the x- and z-directions, respectively:

$$\epsilon_{xx} = \frac{\partial u}{\partial x} \tag{8}$$

and

$$\epsilon_{zz} = \frac{\partial w}{\partial z} \tag{9}$$

for the normal components of strain ϵ.

The shear components are equal due to symmetry, so:

$$\epsilon_{xz} = \epsilon_{zx} = \frac{1}{2}\left(\frac{\partial u}{\partial z} + \frac{\partial w}{\partial x}\right). \tag{10}$$

As the DIC provides discrete data on an even grid we simply estimate the gradients using a central differencing scheme, such that:

$$\epsilon_{xx} \approx \frac{u_{n+1,m} - u_{n-1,m}}{2\Delta x}, \tag{11}$$

$$\epsilon_{zz} \approx \frac{w_{n,m+1} - w_{n,m-1}}{2\Delta z} \tag{12}$$

and

$$\epsilon_{xz} \approx \frac{1}{2}\left(\frac{u_{n,m+1} - u_{n,m-1}}{2\Delta z} + \frac{w_{n+1,m} - w_{n-1,m}}{2\Delta x}\right), \tag{13}$$

where ϵ_{xx} is the strain at the location (n, m). Note that $\Delta x = \Delta z$ as the PIV interrogation windows are square (where Δx and Δz are the spacing between the vectors in the x and z directions, respectively). The error introduced by the discretisation of the equations is second order, $O(\Delta x^2)$.

3. Results

The same experiment was carried out four times; each had the same gelatine concentration, volume and injection method, but a different imaging techniques was applied (see Table 1). Across the different techniques, we have identified four stages of dyke growth to eruption: 1) dyke inception, 2) dyke propagation, 3) pre-eruption ascent and 4) fissure eruption. The appearance of these different stages is now described in detail for each technique.

3.1. Dyke propagation geometry and sub-surface stress

A penny-shaped water-filled fracture was produced during injection. This experimental dyke propagated vertically ($\pm 10°$) towards the surface. Although qualitative, polarised light is very useful to

Fig. 3. Dyke growth in length and width over time, showing three stages of dyke intrusion: a) Dyke length and width, and b) dyke length velocity. Data from two equivalent experiments are shown (see Table 1) up to the point of eruption, measured from the base of the injector. Stage 4 is not shown, but occurs at the end of the experiment as the dyke erupts.

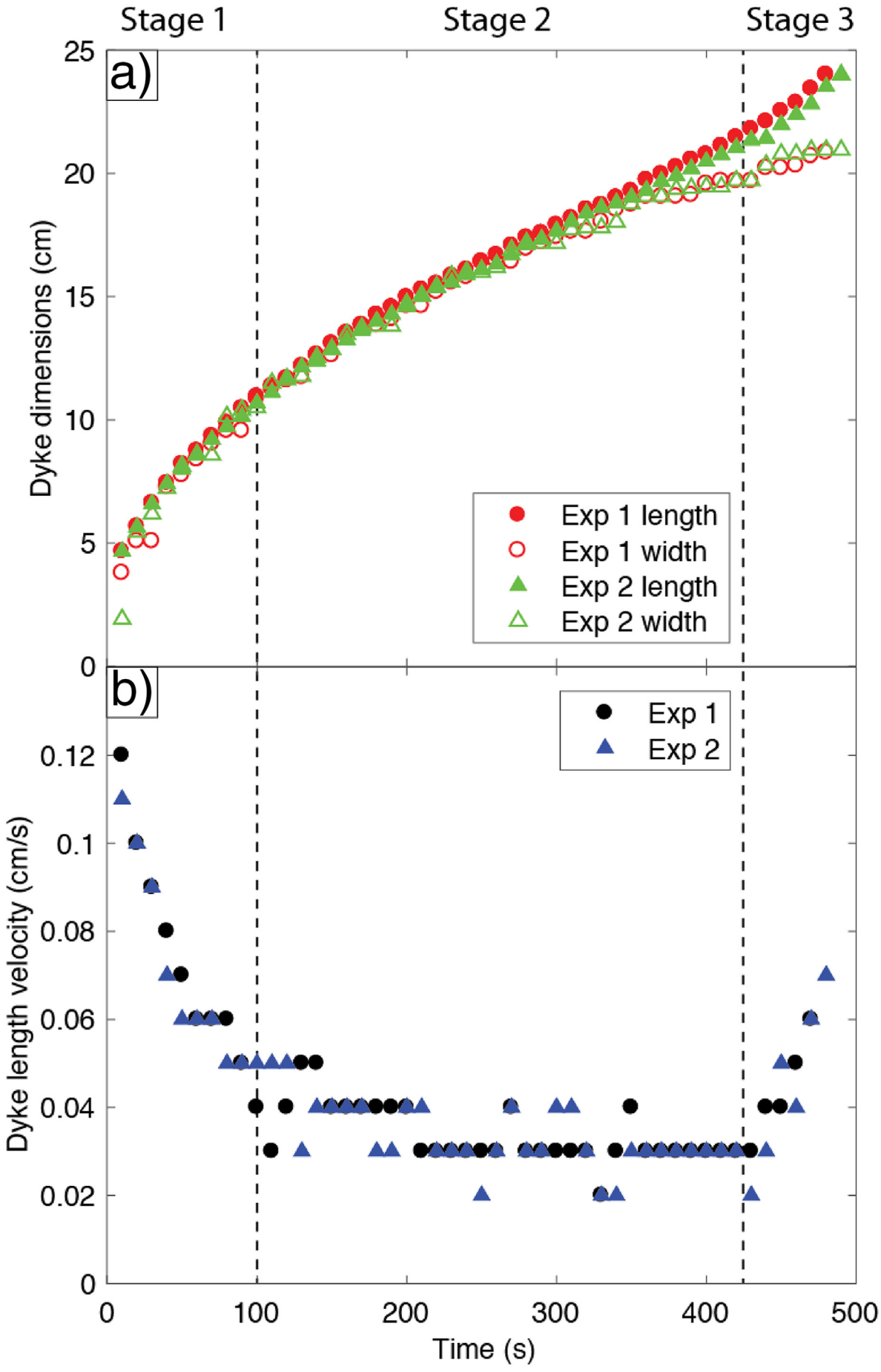
Stage 1
Stage 2
Stage 3
a)
Dyke dimensions (cm)
Exp 1 length
Exp 1 width
Exp 2 length
Exp 2 width
b)
Exp 1
Exp 2
Dyke length velocity (cm/s)
Time (s)

demonstrate the evolving stress field during dyke propagation using the photoelastic properties of gelatine. Coloured fringes depict stress contours, with high concentration of these indicating increasing stress intensity. The developing stress field and its distribution around the growing dyke is shown in Fig. 2 and Supplementary Video Fig. S1, showing stress is concentrated at the dyke tip and producing a 'bow-tie' of stress contours in the x-z plane (Fig. 2i and ii). The visually-stressed region of gelatine is initially localised (Fig. 2ai,ii), but increases in extent as the dyke ascends (Figure 2bi,ii). Towards the surface, the stress field begins to intersect the surface and this continues to eruption (Fig. 2ci,ii).

Three stages of pre-eruption dyke growth can be identified based on the growing dyke geometry. Dyke length and width measurements based on HD video images are shown in Fig. 3a. In Stage 1 a circular geometry is developed (Fig. 2aiii), and this corresponds with approximately equal dyke length and width (Fig. 3a) although the rate of their growth decelerates over approximately the first 100 s of the experiment (Fig. 3b). In Stage 2, the dyke length and width continue to steadily grow at approximately constant velocity (Fig. 3b). Stage 3 marks the lead up to eruption, where the dyke begins to accelerate towards the surface, its length increases at a faster rate than its width, and it develops an elliptical geometry towards eruption (Fig. 2iii,c). At stage 4 the dyke tip reached the surface and it erupted to form a short fissure, and fluid was extruded onto the gelatine surface. The fissure measured approximately 5 cm in length, and the fissure margins were practically closed with an opening <0.1 mm through which fluid flowed. The data presented in Fig. 3 are from two identical experiments (Table 1), and they demonstrate the high degree of reproducibility between experiments.

3.2. Mapping fluid flow within a propagating and erupting dyke

In PIV experiments, passive tracer particles suspended in the injected fluid fluoresced in the y-z plane of the experimental dyke (see Supplementary Video Fig. S2a). Based on the fluid dynamics, the dyke propagation can be described in four stages (see Fig. 4 and Supplementary Video Fig. S2b):

Stage 1: Fluid flow vectors within the first minute of experimental dyke growth were complex, but organised into two jets; one making a curved trajectory that is clockwise near the base of the injector, and the other moving in an anti-clockwise direction in the upper part of the dyke at the dyke margin (Fig. 4a). At this time the dyke was small (approximately 70 mm wide and 70 mm high), far from the gelatine surface (160 mm depth) and close to the injector, with a maximum flow velocity of 14.6×10^{-3} m/s.

Stage 2: After the initial dyke growth, the dyke fluid flow stabilises into one pseudo-steady, upward rising jet along the centre of the dyke (Fig. 4b). Flow velocities are maximum close to the injector, but the maximum flow speed has reduced to 6.6×10^{-3} m/s compared to stage 1. Flow vectors at the growing tip fan out and rotate to flow downwards at the dyke margin. The slowest flow velocities occur in two elliptical regions between the upward-flowing channel and the downflowing margin, where the fluid is almost static.

Stage 3: As the dyke approaches the surfaces to erupt, an instability develops in the flow. The central, upward jet meanders from side to side and at the base the fluid flow comprises two upward jets (Fig. 4c). The fastest moving fluid has migrated away from the injector and occupies a central band within the growing dyke, with slower velocities at the vertical tip and continued down-flow at the dyke margins. The maximum flow velocities in Stage 3 have slightly increased compared to stage 2 and are up to 6.9×10^{-3} m/s. The two elliptical, almost-static, fluid regions between the upward jet and dyke margin remain and have grown in size.

Stage 4: The final stage of dyke ascent is the fissure eruption (Fig. 4d) when the flow dynamics within the dyke dramatically change. At the onset of eruption, all flow vectors are rapidly re-oriented upwards and towards the small fissure that formed in the gelatine surface. The upward jet from the injector and two jets at its base remain, though the region of static fluid rapidly increase in size from depth upwards. The fastest flow velocities of all dyke ascent stages are recorded, reaching 32.2×10^{-3} m/s as fluid is rapidly expelled and the dyke is drained.

3.3. Sub-surface incremental strain evolution during dyke ascent

In DIC experiments, passive-tracer particles within the gelatine solid were illuminated in the x-z plane presenting a cross-section around the growing experimental dyke (see Supplementary Video Fig. S3). The laser-illuminated plane reveals sharp margins of the dyke as it grows, and offers the opportunity to record in detail the evolving cross-sectional thickness variation as the dyke grows; in addition to quantifying the evolving incremental strain (ϵ_{xx}, ϵ_{zz} and ϵ_{xz}) using DIC. Based on the dyke thickness change and evolution in incremental strain, we identify four stages of dyke growth (Fig. 5):

Stage 1: Sub-surface deformation of the gelatine during the early stages of dyke growth show the incremental strain is concentrated at the growing tip (Fig. 5a, 55 s). No incremental strain is recorded at the dyke tail region, indicating its opening is maintained. Vector arrows show the gelatine is displaced predominantly at the dyke margins, radiating from the growing tip, with larger lateral than vertical displacement. The largest component of incremental strain occurs in the horizontal direction (ϵ_{xx}); both vertical (ϵ_{zz}) and shear (ϵ_{xz}) components of strain are small. Overall incremental strain intensity in the early stages of dyke growth spans -2 - 12×10^{-3} ϵ_{xx}, -2 - 3×10^{-3} ϵ_{zz}, and -2 - 3×10^{-3} ϵ_{xz}. Local positive ϵ_{xx} occurs at the dyke tip and local negative ϵ_{xx} occurs adjacent to the dyke tip, whereas local positive ϵ_{zz} occurs just below the dyke tip and local negative ϵ_{zz} just above this. Shear strain is also measured around the dyke tip.

Stage 2: As the dyke ascends, incremental strain continues to be concentrated at the growing tip and displacement arrows show continued outward radial movement at the dyke head with greater lateral than vertical displacement (Fig. 5b, 205 s). Similar patterns of ϵ_{xx}, ϵ_{zz} and ϵ_{xz} occur compared to Stage 1, however their values have all slightly decreased. Uplift of the gelatine free surface is detected by a region of negative ϵ_{zz} developing at the surface. Deflection of the dyke tip from vertical occurs as the dyke begins to propagate in an inclined plane, and this is when an asymmetrical pattern of incremental shear strain (ϵ_{xz}) is detected (lower negative ϵ_{xz} occurs in the upper-right of the dyke tip relative to the lower-left). A small area of negative incremental strain ϵ_{xx} occurs at the dyke tail region. The raw experimental image shows the tail of the dyke has pinched closed. In this stage of dyke propagation: ϵ_{xx} ranges from -1 - 7×10^{-3}, ϵ_{zz} ranges from -1 - 2×10^{-3}, and ϵ_{xz} ranges from -1.5 - 1.5×10^{-3}.

Stage 3: Shortly prior to the dyke erupting, the dyke tip remains the focus of incremental strain; but, the magnitude and extent of the strain components significantly changes. The largest strain values are now in ϵ_{zz} rather than ϵ_{xx}. The intensity of negative vertical incremental strain (ϵ_{zz}) has increased in magnitude and extent. Asymmetry in negative ϵ_{xx} is detected at the dyke tip, and asymmetry in ϵ_{xz} remains. Small amount of incremental shear strain are detected at the gelatine's free surface. Overall in stage 3: ϵ_{xx} ranges from -1 - 5×10^{-3}, ϵ_{zz} ranges from -6 - 12×10^{-3}, and ϵ_{xz} ranges from -1 - 1.5×10^{-3}.

Stage 4: The moment immediately prior to dyke eruption is recorded as opening at the surface and the largest values of ϵ_{xx} are then produced during the experiment. Displacement vectors are oriented towards the

Fig. 4. Four stages of fluid flow within a propagating experimental dyke (Experiment 3), quantified using PIV. Flow velocities (m/s) are shown as vectors (black arrows) and magnitude (colour map). See Supplementary Video S2. a) Stage 1: initial growth (frame 500, 56 s), b) Stage 2: established dyke (frame 2000, 225 s), c) Stage 3, instability development in jet (frame 3500, 396 s), and d) Stage 4: fissure eruption (frame 3691, 416 s).

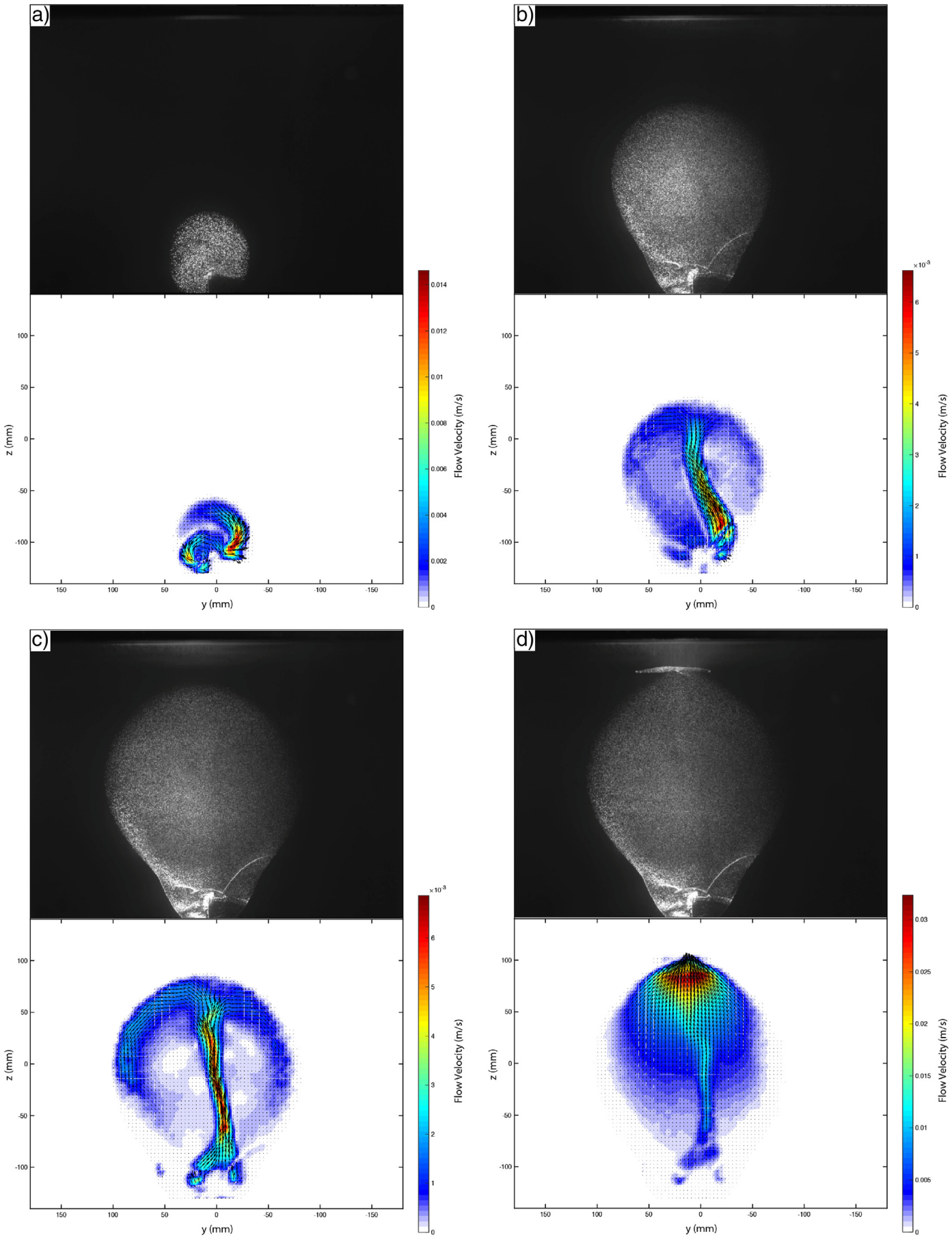
a)
b)
c)
d)
z (mm)
y (mm)
Flow Velocity (m/s)
100
50
0
-50
-100
150
100
50
0
-50
-100
-150
0.014
0.012
0.01
0.008
0.006
0.004
0.002
0
×10-3
6
5
4
3
2
1
0
0.03
0.025
0.02
0.015
0.01
0.005
0

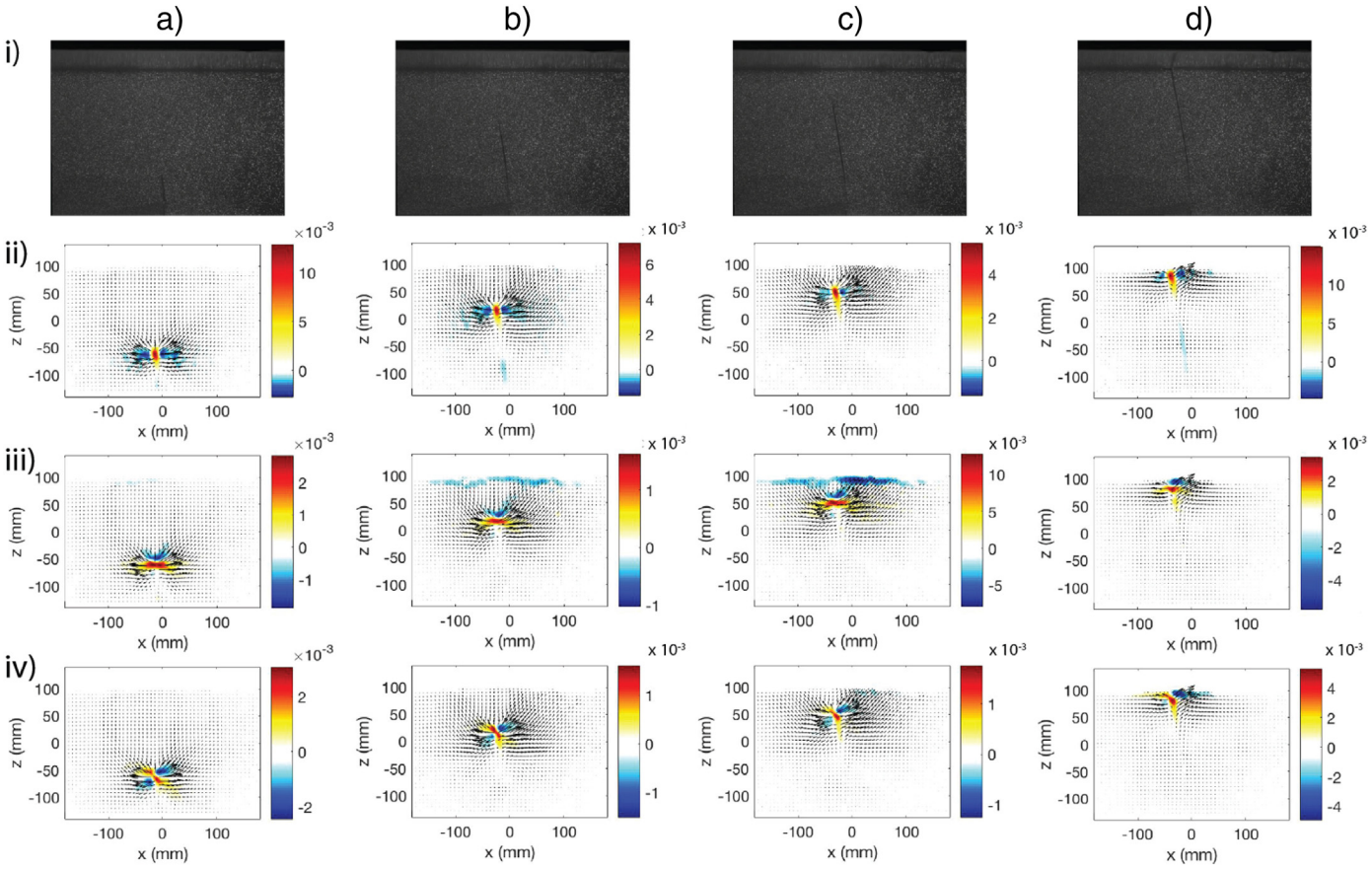

Fig. 5. Four stages of sub-surface incremental strain evolution (colour maps) of experimental dyke ascent to eruption (Experiment 4): i) the de-warped experimental images, ii) ϵ_{xx}, (iii) ϵ_{zz} and (iv) ϵ_{xz}. Displacement is indicated (black arrows), and the DIC analysis is averaged over 10 frames. See Supplementary Video S3. a) Stage 1, dyke inception (frames 55–64, 55 s), b) Stage 2, dyke growth and ascent (frames 205–214, 205 s), c) Stage 3, immediately prior to eruption (frames 400–409, 400 s), and d) Stage 4, fissure eruption (frames 405–414, 405 s).

surface. Progressive 'zipping' closed of the tail occurs as displacement vectors rotate inwards at depth where small, localised regions of negative ϵ_{xx} are produced. The largest incremental strain occurs in the horizontal component (ϵ_{xx}), followed by the shear strain ϵ_{xz} (which is at its largest at stage 4) and then ϵ_{zz} as the dyke completes its path to the surface. During this stage of dyke ascent ϵ_{xx} ranges from -4 - 14×10^{-3}, ϵ_{zz} ranges from -5 - 3×10^{-3}, and ϵ_{xz} ranges from -5 - 5×10^{-3}.

3.4. Surface deformation during dyke ascent

Fig. 6 shows the progressive deformation of the gelatine surface during an experiment as the dyke approached the surface. There was no change in surface topography detected during the majority of dyke ascent (see Supplementary Video Fig. S1c), and it was only when the dyke tip reached approximately <4 cm depth (during the final 120 s of ascent, see Fig. 6a) that an elevation change of the free-surface occurred. By the onset of fissure eruption, there was a gradual overall increase in elevation of 0.5 mm across the whole plane that was monitored. Local topographic highs (up to 1.5 mm) developed either side of the dyke tip (Fig. 6a). The elevation change was relatively broad early on, but became increased and focused as the dyke tip approached the surface. The dyke became slightly deflected from its vertical path (as is common in the experiments, e.g. Experiment 2, Fig. 5), as shown by an increase in the tip position relative to the injector (Fig. 6b). This slightly inclined propagation path resulted in the cumulative surface elevation change not being symmetrical, as the 'hanging wall' of the dyke developed a larger topography (up to 1.5 mm cumulative displacement) than the 'footwall' (approximately 0.9 mm of cumulative displacement).

4. Discussion: Coupled processes during dyke ascent and eruption

Most dykes in nature do not erupt (Gudmundsson, 2002) and the majority of magmas stall within the crust (Crisp, 1984). Determining if magma will breach the surface is of primary concern for volcanic hazard assessments. Dyke ascent in nature can be studied during ascent or post-emplacement; however, in both cases visualising the three-dimensional evolving geometry of the dyke is challenging and requires extrapolation from often two-dimensional datasets (Kavanagh, 2018). Evidence of magma flow, crust deformation and dyke eruption is only partially recorded. Our laboratory experiments can help inform the interpretation of natural data and challenge existing numerical models of dyke ascent.

4.1. Synthesising laboratory experimental results

The range of laboratory experiment monitoring techniques we have employed arguably represent the most detailed and comprehensive description and analysis of coupled fluid flow and host deformation during experimental dyke ascent to eruption. Dyke propagation involves the intrusion of a fluid into a solid, and our results emphasise the strong coupling between the intruding fluid and the deformation of its host-material that influences magma ascent dynamics.

Four common stages of dyke ascent leading to eruption are evident in the experiments. 1) During dyke inception and its early growth, the fluid flow patterns are complex and comprise two circulating fluid jets. Strain is focused at the upper dyke tip as the penny-shape crack is progressively established. 2) As the dyke grows, the fluid flow within it stabilises into a single, rapid and upward flowing jet as the dyke grows in length and width at a constant and steady rate. 3) As the dyke

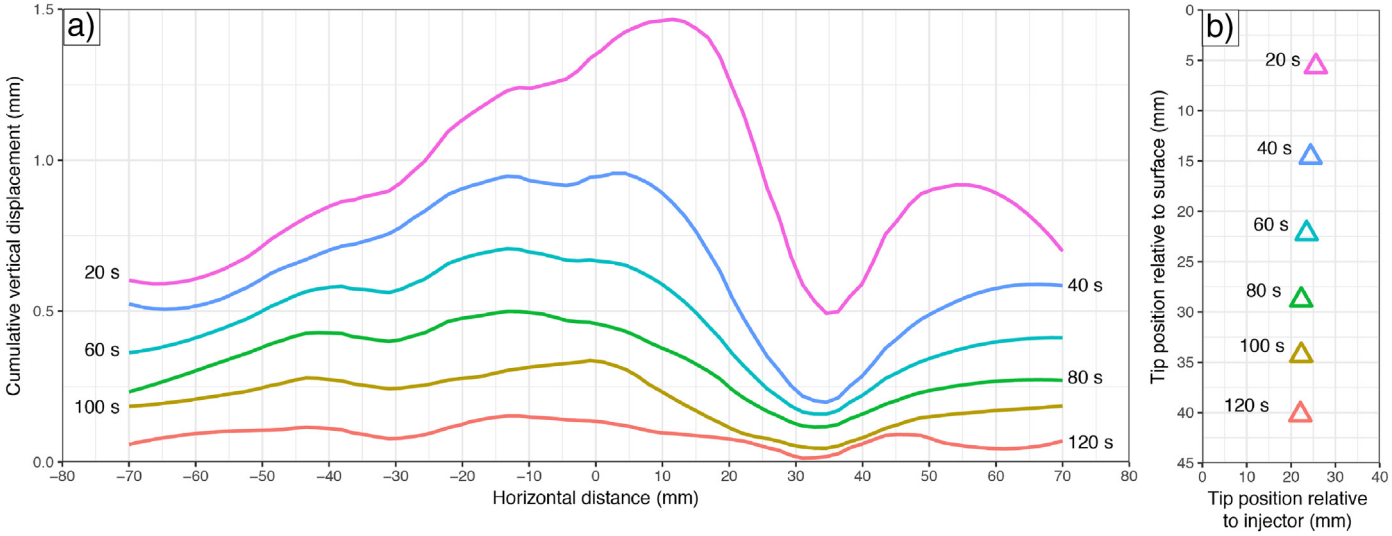

Fig. 6. A series of surface deformation profiles according to dyke tip position of Experiment 1: a) Cumulative surface deformation from 120 to 20 s prior to eruption, where asymmetric topographic highs are produced either side of the dyke tip as it approaches eruption. b) Depth and lateral position of the dyke tip at 20 s intervals before eruption, noting that the tip has gradually deviated from vertical (0 mm) by up to 25.6 mm at 20 s prior to eruption.

approaches the surface our experiments show a fluid instability develops, causing the upward jet to meander and two jets to form at the dyke base. The origin of this instability is not clear, although its appearance corresponds with the time when the dyke tail pinches almost-closed, and when the dyke tip accelerates towards the surface. It is also at this stage that surface deformation is first recorded, resulting in the progressive increase in topography and elevation highs developing above the ascending dyke tip. 4) During dyke eruption, a small fissure is formed at the gelatine surface, a dramatic pressure release induces the rapid evacuation of fluid from the dyke, and the dyke walls 'zip' closed from the tail to the surface.

4.2. Challenging dyke ascent models

The patterns of surface elevation change we measured during dyke ascent agree well with that expected by analytical elastic models; the deformation comprised elevated regions either side of the dyke tip, with a relative low directly above it. Measurements of surface deformation at volcanic centres are often inverted for the source depth and source geometry using simple analytical models that assume intrusion into an isotropic, elastic host-rock. Our experimental observations therefore have the potential to be used to bench-mark these inverse models and inform their development.

The numerical models of dyke ascent that have been published can be divided into two end-member approaches (see Rivalta et al., 2015 for a review). Firstly, there are buoyancy-driven dyke ascent models that emphasise elasticity of the intruded media and its fracture toughness. In these models, the dyke becomes disconnected from its source (e.g. Weertman, 1971). Secondly, there are flux-driven dyke ascent models where the dyke is connected to its source and the fluid dynamics of the intrusion are described by applying lubrication theory (e.g. Lister, 1990a, 1990b; and Spence et al., 1987). The circulation of fluid we observe in the experiments agrees well with the flow pattern expected by Dahm's (2000) dyke model, which emphasises the role of elasticity and fracture toughness but also reconciles the fluid dynamics of the intruding magma. However, this flow pattern contrasts with Roper and Lister (2007) who couple fluid flow and host deformation using lubrication theory and a dyke-scale process zone. Their model anticipates that, when connected to the source, dyke fluid flow should be predominantly vertical inside the dyke. However, our results suggest that, despite not having attained their 'buoyant length' and only having a small density contrast between intruding fluid and intruded host, our experimental dykes have the ascent dynamics expected of buoyant fluid-filled fractures in an elastic material, where the mechanical properties of the intruded host dominate the growth dynamics and the viscous resistance of the fluid to flow is minimal.

In our experiments, fluid is driven into the dyke at a constant volumetric flux and the dyke remains connected to its source. According to Linear Elastic Fracture Mechanics, the fluid-filled crack will propagate when the fluid overpressure exceeds the fracture pressure P_f of the gelatine solid (Lister and Kerr, 1991):

$$P_f = \frac{K_c}{\sqrt{\pi l}}, \tag{14}$$

where K_c is the fracture toughness of the gelatine and l is the crack length. Gelatine's K_c can be estimated by the relationship (Kavanagh et al., 2013):

$$K_c = 1.4\sqrt{E}. \tag{15}$$

In our experiments, $E = 2000$–3000 Pa and so we estimate $K_c = 63$–77 Pa $m^{1/2}$. However, the density difference between the injected fluid and the intruded gelatine also results in a buoyancy pressure P_b (Rubin, 1995):

$$P_b = \left(\rho_s - \rho_{liq}\right) g L_b, \tag{16}$$

where ρ_s is the density of the solid (gelatine), ρ_{liq} is the density of the liquid (water), g is gravity and L_b is the buoyant length of the dyke (Eq. 2) (Taisne and Tait, 2009). Following these relationships, the calculated buoyant length of our experimental dykes is 1.3–1.4 m, where $\rho_s = 1002.5$ kg/m^3, $\rho_{liq} = 998$ kg/m^3 and $g = 9.81$ m/s, which is much greater than the height of the experimental tank (0.3 m). It is therefore expected that the growth of our experimental dykes is flux-driven, and any buoyancy effects should be minimal.

The experimental dyke geometry in profile is circular in the early stages of dyke growth. This penny-shaped geometry is a consequence of intrusion into a homogeneous, isotropic elastic solid; in nature, however, anisotropy and mechanical heterogeneities of the crust are expected to influence the shape of the dyke (e.g. Kavanagh and Sparks, 2011). Fluid may also be fed into the dyke by a slit-like geometry rather than the nozzle-like injector we used. The dyke geometry evolved to become elongate as it approached the surface, in response to an

accelerating dyke tip. In nature, mechanical heterogeneity of the crust will likely affect the dyke ascent rate and whether or not such an acceleration would occur. In cross-section, our experimental dyke developed a pinched tail and 'teardrop' morphology as the dyke propagated through the tank towards eruption. This geometry is similar to that expected of a 'Weertman crack', where a fixed volume injection ascends buoyantly though an elastic material (Weertman, 1971). This geometry occurred despite the crack receiving a constant flux of fluid, and remaining connected to the source (even if the connection is very small). Our experimental results therefore suggest the Weertman-crack geometry is not restricted to fixed volume injections, but can be developed by dykes that have sustained magma flux too. The analytical models that describe the buoyant length of fluid-filled fractures propagating in an elastic material therefore may not fully capture the dynamical processes of dyke ascent, and so will need to be revisited in the context of these new experimental observations.

4.3. Magma flow in nature

Our understanding of the dynamics of magma flow in dykes is limited to observations of volcanic fissure eruptions (e.g. Lundgren et al., 2013); in the early stages of eruption the magma exits along the fissure length, but rapidly the extrusion becomes focused at a few vents due to flow channelisation. The crystalline magma within ancient, solidified dykes offers the best access to the dyke; however, exposure is often limited to partial 2-dimensional sections and unravelling *syn*- and post-emplacement textures from the time-sequence of magma solidification is difficult. However, there are several macroscopic flow indicators that can be used, including elongated vesicles that are aligned (e.g. Fig. 7), scour marks (e.g. Smith, 1987), phenocryst alignment (e.g. Bhattacharji and Smith, 1964), drag folds (e.g. Walker et al., 2017) and cataclastic elongation of phenocrysts (Smith, 1987). Magnetic fabrics, such as AMS have also been used to infer magma flow (e.g. Herrero-Bervera et al., 2001). Temporal variations in flow are postulated based on, for example, bubble-rich and bubble-poor coupled bands that suggest pressure fluctuations (see Fig. 7c and d). Any flow indicator needs to be used with caution, especially as the final stages of magma flow may be drainage or back-flow towards the source (e.g. Lundgren et al., 2013).

Our experimental results of the vectors of fluid flow during dyke intrusion and eruption provides important dynamical constraints that will likely aid the interpretation of flow fabrics within intrusions, in particular due to the identification of distinct stages of dyke ascent leading to eruption. In our experiments, the fluid initially circulated in two jets as the pre-cut was first filled and then the crack began to propagate. This early flow pattern was potentially an artefact of the initial injection

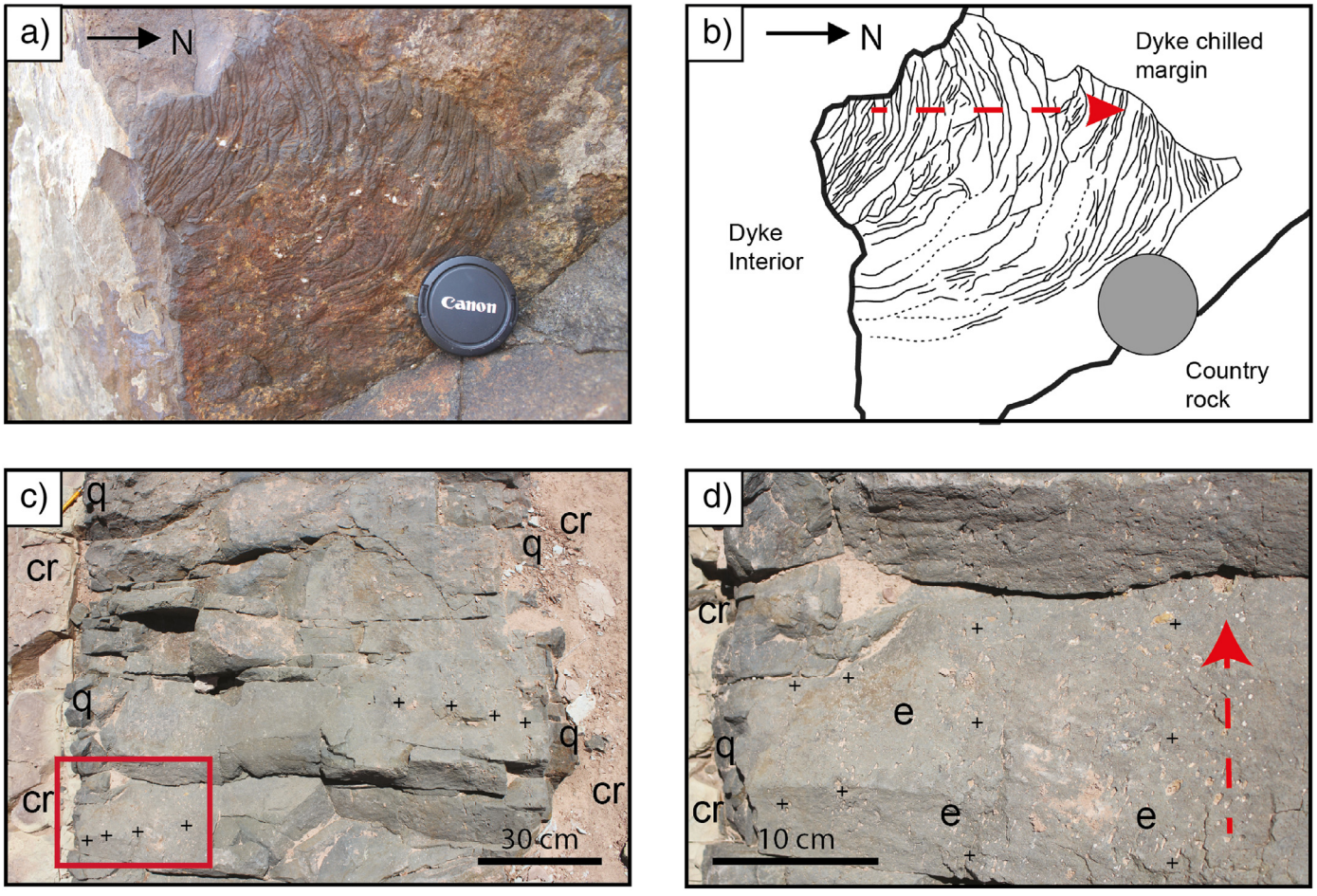

Fig. 7. Field-scale features where orientations of magma flow are preserved within solidified dykes in different planes. a) Dyke's y-z plane: Photograph of a quarry face showing a basaltic dyke margin (Isle of Skye, Scotland); the country rock has eroded away to reveal ropey structures preserved at the contact. b) Complementary sketch diagram of a): ropey structures (thin-solid and thin-dashed lines) on the dyke chilled margin, and the inferred local palaeo-flow direction (red dashed arrow). c) Dyke's x-y plane: Photograph of a complete cross-section of a basaltic dyke viewed from above (San Rafael subvolcanic field, Utah); quenched (q) chilled margins against the country rock (cr), and cm-thick vesicle-rich bands (+) that are bound by vesicle-poor bands and parallel to the dyke margins. The position of the zoomed image (d) is indicated (red box). d) Zoomed photograph of c) additionally showing the location of elongated vesicles (e) within the dyke interior.

conditions, and could have formed by the injector being partially blocked by incomplete breaking of the petroleum jelly seal. This first stage in the experimental dyke growth could vary between experiments, and so directly comparing this early stage of the experiment with natural observations is not recommended. However, after this initial stage the dyke width and length increased at constant velocity and this was when we observed a single jet to form and circulation of fluid within the propagating dyke. This jet persisted from these early stages of dyke growth up to immediately prior to eruption, with rapid evacuation of the dyke when it breached the surface. Our experimental observations therefore suggest that fluid flow trajectories within a non-feeder dyke (that does not erupt) may be highly variable with upward, lateral and downward flow occurring. These would therefore be distinct from a feeder dyke where the flow velocity would be predominantly vertical, proffering the opportunity to assess whether or not a dyke erupted (even with limited exposure of the plumbing system) based on the flow vectors preserved but also depending on the timescale of solidification (e.g. Daniels et al., 2012). Jet formation and channelisation within natural dykes may occur in nature, resulting in progressive and preferred erosion of the country rock due to the sustained and rapid fluid flow, leading to the development of asymmetrical dyke geometries in the rock record (e.g. Kavanagh and Sparks, 2011). Variations in flow, either during intrusion or eruption, may lead to erosion of the mushy and progressively crystallising dyke margins. Our experimental dykes comprised a low viscosity Newtonian fluid, however during magma ascent it is likely that non-Newtonian fluid rheology such as shear-thinning will develop as the crystal and bubble-content of the magma increases. Future experiments will be required to assess the impact of non-Newtonian rheologies on the flow dynamics within a propagating dyke.

4.4. Host-rock deformation in nature

The conceptual framework used in our laboratory study is that dykes can be modelled as hydraulic fractures that intrude an elastic material, which is in-keeping with assumptions used during real-time monitoring and inversion modelling of intrusion-induced deformation at active volcanoes. However, an important consideration in dyke ascent mechanics is understanding under what circumstances they create their own fractures or instead intrude pre-existing weak planes. This is important for hazard assessment and predicting the sites of future vents from dyke ascent e.g. in a monogenetic volcanic field (e.g. Le Corvec et al., 2013b). The sub-surface deformation patterns we observe in our experiments, such as incremental strain and stress field evolution, could be helpful to interpret seismicity during active intrusion. The surface deformation patterns could be helpful to inform the interpretation of tilt meter data, GPS monitoring networks and InSAR analysis.

Field evidence of host deformation associated with dyke ascent ranges from macro- to micro-scale. Dyke-parallel fractures at the dyke margins within sedimentary (Delaney et al., 1986) or igneous host-rocks (Brown et al., 2007; Kavanagh and Sparks, 2011) may suggest these were pre-existing structures that were exploited by the ascending magma, although the exploitation of existing fractures is likely to be a relatively near-surface process (Rubin, 1995). A potentially valuable, yet unexplored, tool to study the micro-scale damage zone surrounding hydraulic fractures (e.g. dykes) are Fluid Inclusion Planes (FIPs). FIPs appear under optical microscopy as small linear "bubble" trails in individual crystals and are thought to be fossilised microfractures which are the result of healing, or "necking down" of previously open fractures which functioned as fluid pathways (Roedder, 1984). FIPs can provide valuable information when studying rock deformation as they can provide insight into deformation geometries, chronology of deformation (Lespinasse, 1999; Pecher et al., 1985) and are potential indicators to the paleostress field (Lespinasse and Pecher, 1986). The healing process is relatively quick in relation to geological time (Smith and Evans, 1984) and they form as Mode I fractures, occur predominately perpendicular to the least principal compressive stress axis, σ^3, with no evidence of shear displacement which would be expected from Mode II/III fractures (Lespinasse, 1999). Quartz is a common mineral for FIPs to be observed as, due to its crystallographic properties, fractures in quartz are usually formed in response to the regional stress field (Lespinasse and Cathelineau, 1990). Minerals such as feldspars, however, which have more complex cryptographic features, such as twinning and the presence of cleavages, can alter the preservation or have preferred orientations of FIPs (Lespinasse, 1999). Observations of FIPs can be made optically at magnifications as low as ×10, as shown in Fig. 8a; however optical observations are somewhat hindered due to the healing process, making many FIPs invisible in plane polarised and cross polarised light. The use of a Scanning Electron Microscope fitted with a Cathodoluminescent detector (SEM-CL) can dramatically increase the number of observable FIPs by up to 100% in some cases. This is demonstrated in the optical micrograph Fig. 8a, which shows roughly 8 visible FIPs, compared to the SEM-CL micrograph Fig. 8b, which has 16 potential FIPs. The SEM-CL provides a more complete image of FIPs, making it a more effective structural tool to assess host-rock damage around dykes.

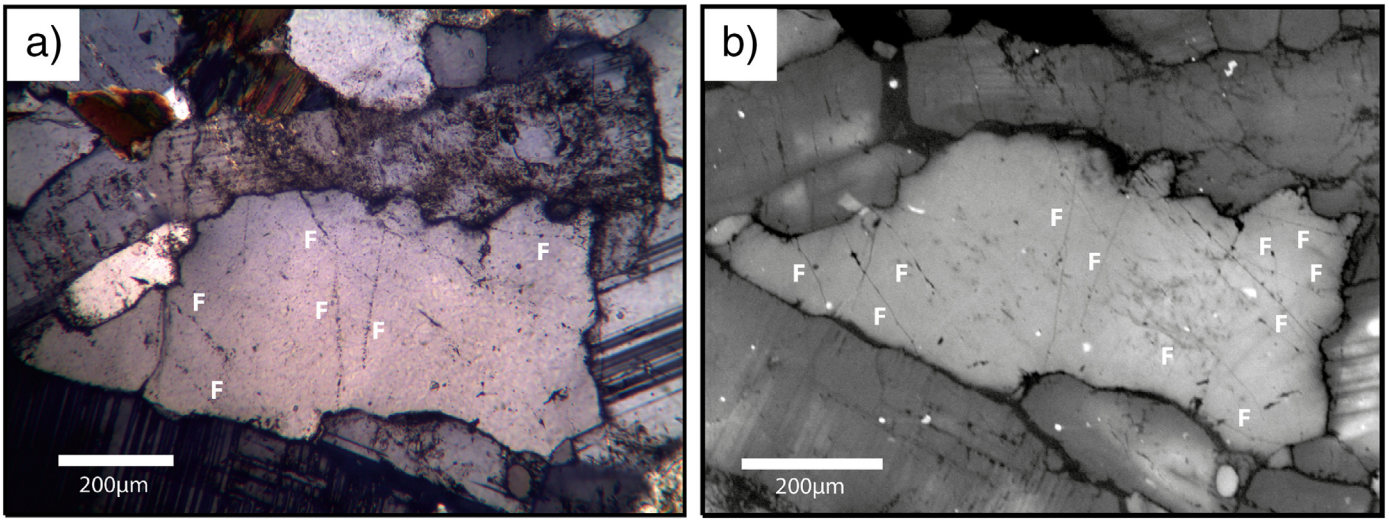

Fig. 8. a) Optical photomicrograph in cross polarised light showing fluid inclusion planes (F) within quartz. b) SEM-Cathodoluminescent image showing comparative view of microfractures visible, note the increased detail and abundancy of FIPs (F).

5. Conclusions

The laboratory methods we have employed have allowed the detailed description and quantification of coupled fluid flow and host deformation during the inception, growth and eruption of an experimental dyke. We have identified four phases of dyke ascent:

Stage 1: Dyke inception and early growth. Fluid flow is complex, circulating as the dyke grows equally in breadth and length creating a penny-shaped geometry. Sub-surface deformation is focused at the growing tip, with material at the dyke tip margin progressively displaced outwards, and stress concentration showing a 'bow-tie' geometry. No surface elevation change is recorded as the dyke is formed and begins to grow.

Stage 2: Dyke propagation. Fluid flow comprises a rapid, centralised, upward-rising, pseudo-steady jet with slow down-welling at the dyke margin. Regions of static fluid develop within the circulating flow. Sub-surface deformation remains concentrated at the growing tip, shown by a concentration in incremental strain and stress. The dyke tail pinches almost-closed at depth at the end of this stage.

Stage 3: Near-surface ascent. A flow instability develops as the upward and centralised rapid fluid flow begins to meander and move from side to side. Two jets at the base of the dyke feed into the upper single jet, and slower fluid continues to down-well at the growing dyke margin. The dyke begins to lengthen, developing an elliptical geometry as the dyke tip begins to accelerate towards the surface. The pinched tail of the ascending dyke migrates towards the surface. The dyke trajectory is deflected as shear stresses intensify, and the dyke stress field begins to interact with the surface. The inclined dyke produces an asymmetrical cumulative elevation change centred above the dyke.

Stage 4: Fissure eruption. Rapid opening of the dyke occurs as it intersects the surface and produces a short fissure. This depressurisation causes rapid evacuation of fluid from the dyke. Flow is focused towards the vent and the active-region of flow is increasingly focused towards the surface as the pinched dyke tail zips closed from depth and accelerates towards the surface.

The experimental results emphasise the importance of considering coupled fluid flow and host deformation when developing the next generation of dyke ascent models, to inform the interpretation of the field and geophysical evidence of ancient, ongoing, and future dyke intrusion events.

Supplementary data to this article can be found online at https://doi.org/10.1016/j.jvolgeores.2018.01.002.

Acknowledgements

JLK and DJCD acknowledge 'Living With Environmental Change' pump priming grants from the University of Liverpool, and a Natural Environment Research Council Research Experience Placement from the Liverpool-Manchester EAO DTP that funded AJB (NE/L002469/1). JLK acknowledges a Royal Society grant (RG130771). SHH acknowledges support from the Malaysian Government and the National University of Malaysia. EW thanks a Natural Environment Research Council Liverpool-Manchester EAO DTP PhD studentship (NE/L002469/1). SM acknowledges support from a Mineralogical Society Postgraduate Student Bursary which funded fieldwork to Skye. All authors thank the University of Liverpool, and Silvio De Angelis and Rob Duller are thanked for their assistance with the Micro Epsilon laser scanner. Sarah Henton De Angelis is thanked for assistance with the SEM and CL. Joan Martí, Lionel Wilson and Tim Horscroft are thanked for the invitation to write this research paper. Carmen López and Agust Gudmundsson are thanked for thoughtful reviews that improved the manuscript, and Joan Martí is thanked for editorial support.

References

Abdelmalak, M.M., et al., 2012. Fracture mode analysis and related surface deformation during dyke intrusion results from 2D experimental modelling. Earth Planet. Sci. Lett. 359–360 (C), 93–105.
Adrian, R.J., 1991. Particle-imaging techniques for experimental fluid mechanics. Annu. Rev. Fluid Mech. 23, 261–304.
Bhattacharji, S., Smith, C.H., 1964. Flowage differentiation. Science 145, 150–153.
Brizzi, S., et al., 2016. Salt matters: how salt affects the rheological and physical properties of gelatine for analogue modelling. 679, 88–101.
Brown, R.J., et al., 2007. Mechanically disrupted and chemically weakened zones in segmented dike systems cause vent localization: evidence from kimberlite volcanic systems. Geology 35 (9), 815–818.
Caricchi, L., et al., 2014a. Frequency and magnitude of volcanic eruptions controlled by magma injection and buoyancy. Nat. Geosci. 7 (2), 1–5.
Caricchi, L., et al., 2014b. The influence of cooling, crystallisation and re-melting on the interpretation of geodetic signals in volcanic systems. Earth Planet. Sci. Lett. 388 (C), 166–174.
Castro, J.M., et al., 2016. Rapid laccolith intrusion driven by explosive volcanic eruption. Nat. Commun. 7, 1–7.
Cervelli, P., et al., 2002. The 12 September 1999 upper east rift zone dike intrusion at Kilauea volcano, Hawaii. J. Geophys. Res. 107 (B7), 2150.
Crisp, J.A., 1984. Rates of magma emplacement and volcanic output. J. Volcanol. Geotherm. Res. 20, 177–211.
Dahm, T., 2000. On the shape and velocity of fluid-filled fractures in the earth. Geophys. J. Int. 142 (1), 181–192.
Daniels, K.A., Menand, T., 2015. An experimental investigation of dyke injection under regional extensional stress. J. Geophys. Res. Solid Earth 120, 2014–2035.
Daniels, K.A., et al., 2012. The shapes of dikes: evidence for the influence of cooling and inelastic deformation. GSA Bull. 124 (7–8), 1102–1112.
Delaney, P.T., et al., 1986. Field relations between dikes and joints: emplacement processes and palaeostress analysis. J. Geophys. Res. 91 (B5), 4920–4938.
Djabourov, M., Leblond, J., Papon, P., 1988. Gelation of aqueous gelatin solutions. II. Rheology of the sol-gel transition. J. Phys. 49 (2), 333–343.
Geshi, N., Kusumoto, S., Gudmundsson, A., 2010. Geometric difference between non-feeder and feeder dikes. Geology 38 (3), 195–198.
González, P.J., Palano, M., 2014. Mt. Etna 2001 eruption: new insights into the magmatic feeding system and the mechanical response of the western flank from a detailed geodetic dataset. J. Volcanol. Geotherm. Res. 274, 108–121.
Gudmundsson, A., 2002. Emplacement and arrest of sheets and dykes in central volcanoes. J. Volcanol. Geotherm. Res. 116, 279–298.
Gudmundsson, A., 2003. Surface stresses associated with arrested dykes in rift zones. Bull. Volcanol. 65 (8), 606–619.
Gudmundsson, A., 2006. How local stresses control magma-chamber ruptures, dyke injections, and eruptions in composite volcanoes. Earth Sci. Rev. 79 (1–2), 1–31.
Gudmundsson, A., et al., 2014. Dike emplacement at Bardarbunga, Iceland, induces unusual stress changes, caldera deformation, and earthquakes. Bull. Volcanol. 76 (10), 869.
Herrero-Bervera, E., et al., 2001. Magnetic fabric and inferred flow direction of dikes, conesheets and sill swarms, Isle of Skye, Scotland. J. Volcanol. Geotherm. Res. 106 (3), 195–210.
Ilyinskaya, E., et al., 2017. Earth and planetary science letters. Earth Planet. Sci. Lett. 1–14.
Kahl, M., et al., 2011. Dynamic plumbing system beneath volcanoes revealed by kinetic modeling, and the connection to monitoring data: an example from Mt. Etna. Earth Planet. Sci. Lett. 308, 11–12.
Kavanagh, J.L., 2018. Mechanisms of magma transport in the upper crust – Dyking. In: Burchardt, S. (Ed.), Volcanic and Igneous Plumbing Systems: Understanding Magma Transport, Storage, and Evolution in the Earth's Crust. Elsevier (In press).
Kavanagh, J.L., Sparks, R.S.J., 2011. Insights of dyke emplacement mechanics from detailed 3D dyke thickness datasets. J. Geol. Soc. 168 (4), 965–978.
Kavanagh, J.L., Menand, T., Sparks, R.S.J., 2006. An experimental investigation of sill formation and propagation in layered elastic media. Earth Planet. Sci. Lett. 245 (3–4), 799–813.
Kavanagh, J., Menand, T., Daniels, K.A., 2013. Gelatine as a crustal analogue: determining elastic properties for modelling magmatic intrusions. Tectonophysics 582, 101–111.
Kavanagh, J.L., Boutelier, D., Cruden, A.R., 2015. The mechanics of sill inception, propagation and growth: experimental evidence for rapid reduction in magmatic overpressure. Earth Planet. Sci. Lett. 421, 117–128.
Kavanagh, J.L., et al., 2017a. Controls on sill and dyke-sill hybrid geometry and propagation in the crust: the role of fracture toughness. Tectonophysics 698 (C), 109–120.
Kavanagh, J.L., Engwell, S., Martin, S., 2017b. A review of analogue and numerical modelling in volcanology. Solid Earth Discussions. https://doi.org/10.5194/se-2017-40.
Le Corvec, N., Menand, T., Lindsay, J., 2013a. Interaction of ascending magma with pre-existing crustal fractures in monogenetic basaltic volcanism: an experimental approach. J. Geophys. Res. Solid Earth 118 (3), 968–984.
Le Corvec, N., Spörli, K.B., et al., 2013b. Spatial distribution and alignments of volcanic centers: clues to the formation of monogenetic volcanic fields. Earth Sci. Rev. 124 (C), 1–19.
Lespinasse, M., 1999. Are fluid inclusion planes useful in structural geology? J. Struct. Geol. 21, 1237–1243.
Lespinasse, M., Cathelineau, M., 1990. Fluid percolations in a fault zone: a study of fluid inclusion planes in the St Sylvestre granite, northwest massif central, France. Tectonophysics 184, 173–187.
Lespinasse, M., Pecher, A., 1986. Microfracturing and regional stress field: a study of the preferred orientations of fluid-inclusion planes in a granite from the massif central, France. J. Struct. Geol. 8 (2), 169–180.

Lister, J.R., 1990a. Buoyancy-driven fluid fracture: similarity solutions for the horizontal and vertical propagation of fluid-filled cracks. J. Fluid Mech. 217, 213–239.
Lister, J.R., 1990b. Buoyancy-driven fluid fracture: the effects of material toughness and of low-viscosity precursors. J. Fluid Mech. 210, 263–280.
Lister, J.R., Kerr, R.C., 1991. Fluid-mechanical models of crack propagation and their application to magma transport in dykes. J. Geophys. Res. Solid Earth 96 (B6), 10049–10077.
Lundgren, P., et al., 2013. Evolution of dike opening during the march 2011 Kamoamoa fissure eruption, Kīlauea volcano, Hawai'i. J. Geophys. Res. Solid Earth 118 (3), 897–914.
Maccaferri, F., et al., 2014. Off-rift volcanism in rift zones determined by crustal unloading. Nat. Geosci. 7 (4), 297–300.
Menand, T., Daniels, K.A., Benghiat, P., 2010. Dyke propagation and sill formation in a compressive tectonic environment. J. Geophys. Res. 115 (B08201). https://doi.org/10.1029/2009JB006791.
Menand, T., de Saint-Blanquat, M., Annen, C., 2011. Emplacement of magma pulses and growth of magma bodies. Tectonophysics 500 (1–4), 11–19.
Patane, D., et al., 2002. Tomographic images and 3D earthquake locations of the seismic swarm preceding the 2001 Mt. Etna eruption: evidence for a dyke intrusion. Geophys. Res. Lett. 29 (10), 1497.
Pecher, A., Lespinasse, M., Leroy, J., 1985. Relations between fluid inclusion trails and regional stress field: a tool for fluid chronology—an example of an intragranitic uranium ore deposit (northwest massif central, France). Lithos 18, 229–237.
Pinel, V., Jaupart, C., 2000. The effect of edifice load on magma ascent beneath a volcano. Philos. Trans. R. Soc. A Math. Phys. Eng. Sci. 358 (1770), 1515–1532.
Putirka, K.D., 2017. Down the crater: where magmas are stored and why they erupt. Elements 13, 11–16.
Righetti, R., et al., 2004. The feasibility of using elastography for imaging the Poisson's ratio in porous media. Ultrasound Med. Biol. 30 (2), 215–228.
Rivalta, E., Böttinger, M., Dahm, T., 2005. Buoyancy-driven fracture ascent: experiments in layered gelatine. J. Volcanol. Geotherm. Res. 144 (1–4), 273–285.
Rivalta, E., et al., 2015. A review of mechanical models of dike propagation: schools of thought, results and future directions. Tectonophysics 638, 1–42.
Roedder, E., 1984. Fluid inclusions. Rev. Mineral. 12, 646.
Roper, S.M., Lister, J.R., 2007. Buoyancy-driven crack propagation: the limit of large fracture toughness. J. Fluid Mech. 580, 359–380.
Rubin, A.M., 1995. Propagation of magma-filled cracks. Annu. Rev. Earth Planet. Sci. 23 (1), 287–336.
Sigmundsson, F., et al., 2010. Intrusion triggering of the 2010 Eyjafjallajökull explosive eruption. Nature 468 (7322), 426–430.
Sigmundsson, F., et al., 2014. Segmented lateral dyke growth in a rifting event at Ba´rðarbunga volcanic system, Iceland. Nature 517 (7533), 191–195.
Smith, R.P., 1987. Dyke emplacement at Spanish Peaks, Colorado. In: Halls, H.C. (Ed.), Mafic Dyke Swarms, Geological Association of Canada Special Paper. 34, pp. 47–54.
Smith, D.L., Evans, B., 1984. Diffusional crack healing in quartz. J. Geophys. Res. 89, 4125–4135.
Sparks, R., Biggs, J., Neuberg, J.W., 2012. Monitoring volcanoes. Science 335, 1310–1311.
Spence, D.A., Sharp, P.W., Turcotte, D.L., 1987. Buoyancy-driven crack propagation: a mechanism for magma migration. J. Fluid Mech. 174, 135–153.
Taisne, B., Jaupart, C., 2009. Dike propagation through layered rocks. J. Geophys. Res. Solid Earth 114 (B9). https://doi.org/10.1029/2008JB006228.
Taisne, B., Tait, S., 2009. Eruption versus intrusion? Arrest of propagation of constant volume, buoyant, liquid-filled cracks in an elastic, brittle host. J. Geophys. Res. 114 (B6), B06202.
Taisne, B., Tait, S., 2011. Effect of solidification on a propagating dike. J. Geophys. Res. 116 (B1), B01206.
Takada, A., 1990. Experimental study on propagation of liquid-filled crack in gelatin: shape and velocity in hydrostatic stress condition. J. Geophys. Res. 95, 8471–8481.
Walker, R.J., Branney, M.J., Norry, M.J., 2017. Dike propagation and magma flow in a glassy rhyolite dike: a structural and kinematic analysis. Geol. Soc. Am. Bull. B31378, 1.
Watanabe, T., et al., 2002. Analogue experiments on magma-filled cracks: competition between external stresses and internal pressure. Earth Planets Space 54, 1247–1261.
Weertman, J., 1971. Theory of water-filled crevasses in glaciers applied to vertical magma transport beneath oceanic ridges. J. Geophys. Res. 76 (5), 1171–1183.
Wright, T.J., et al., 2012. Geophysical constraints on the dynamics of spreading centres from rifting episodes on land. Nat. Geosci. 5, 242–250.